spin-polarized because the same number of spin-up and spin-down electrons move in the same direction with the same velocity. In the case of inelastic scattering the current may be polarized.

The uniformity of the spin polarization in space is preserved during the scattering processes. Therefore, the spin-galvanic effect differs from surface currents induced by inhomogeneous spin orientation[25]. It also differs from other experiments where the spin current is caused by gradients of potentials, concentrations and so on, like the spin-voltaic effect[26,27] and the photo-voltaic effect, which occur in inhomogeneous samples, and like the 'para-magnetic metal-ferromagnet' junction or *p-n* junctions. When considering spintronic devices involving heterojunctions, spin-galvanic current must be taken into account. □

Received 3 January; accepted 25 March 2002.

1. Wolf, S. A. *et al.* Spintronics: a spin-based electronics vision for the future. *Science* **294,** 1488–1495 (2001).
2. Hägele, D. *et al.* Spin transport in GaAs. *Appl. Phys. Lett.* **73,** 1580–1582 (1998).
3. Kikkawa, J. M. & Awschalom, D. D. Lateral drag of spin coherence in gallium arsenide. *Nature* **397,** 139–141 (1999).
4. Bychkov, Y. A. & Rashba, E. I. Properties of a 2D electron gas with lifted spectral degeneracy. *Sov. JETP Lett.* **39,** 78–81 (1984).
5. D'yakonov, M. I. & Kocharovskii, V. Yu. Spin relaxation of two-dimensional electrons in noncentrosymmetric semiconductors. *Sov. Phys. Semicond.* **20,** 110–111 (1986).
6. Koopmans, B., Santos, P. V. & Cardona, M. Optical activity in semiconductors: stress and confinement effects. *Phys. Status Solidi* **205,** 419–463 (1998).
7. Ivchenko, E. L., Lyanda-Geller, Yu, B. & Pikus, G. E. Current of thermalized spin-oriented photocarriers. *Sov. Phys. JETP* **71,** 550–557 (1990).
8. Fiederling, R. *et al.* Injection and detection of spin-polarized current in a light-emitting diode. *Nature* **402,** 787–789 (1999).
9. Meier, F. & Zakharchenya, B. P. (eds) *Optical Orientation* 1–523 (Elsevier Science, Amsterdam, 1984).
10. Hammar, P. R. & Johnson, M. Spin-dependent current transmission across a ferromagnet-insulator-two-dimensional electron gas junction. *Appl. Phys. Lett.* **79,** 2591–2593 (2001).
11. Zhu, H. J. *et al.* Room-temperature spin injection from Fe into GaAs. *Phys. Rev. Lett.* **87,** 016601-1–016601-4 (2001).
12. Hanbicki, A. T. *et al.* Efficient electrical spin injection from a magnetic metal/tunnel barrier contact into a semiconductor. *Appl. Phys. Lett.* **80,** 1240–1242 (2002).
13. Tarasenko, S. A. & Ivchenko, E. L. Spin orientation of two-dimensional electron gas under intraband optical pumping. Preprint cond-mat/0202471 at ⟨http://xxx.lanl.gov⟩ (2002).
14. Ganichev, S. D. *et al.* Conversion of spin into direct electric current in quantum wells. *Phys. Rev. Lett.* **86,** 4358–4361 (2001).
15. Hanle, W. Über magnetische Beeinflussung der Polarisation der Resonanzfluoreszenz. *Z. Phys.* **30,** 93–105 (1924).
16. Ganichev, S. D. Tunnel ionization of deep impurities in semiconductors induced by terahertz electric fields. *Physica B* **273–274,** 737–742 (1999).
17. Ivchenko, E. L., Kiselev, A. A. & Willander, M. Electronic *g*-factor in biased quantum wells. *Solid State Commun.* **102,** 375–378 (1997).
18. Damen, T. C. *et al.* Subpicosecond spin relaxation dynamics of excitons and free carriers in GaAs quantum wells. *Phys. Rev. Lett.* **67,** 3432–3435 (1991).
19. Kikkawa, J. M. *et al.* Room-temperature spin memory in two-dimensional electron gases. *Science* **277,** 1284–1287 (1997).
20. Sandu, J. S. *et al.* Gateable suppression of spin relaxation in semiconductors. *Phys. Rev. Lett.* **86,** 2150–2153 (2001).
21. Marie, X. *et al.* Hole spin quantum beats in quantum-well structures. *Phys. Rev. Lett.* **60,** 5811–5817 (1999).
22. Andrianov, A. V. & Yaroshetskii, I. D. Magnetic-field-induced circular photovoltaic effect in semiconductors. *Sov. JETP Lett.* **40,** 882–884 (1984).
23. Ivchenko, E. L., Lyanda-Geller, Yu, B. & Pikus, G. E. Circular magnetophotocurrent and spin splitting of band states in optically-inactive crystals. *Solid State Commun.* **69,** 663–665 (1989).
24. Averkiev, N. S., Golub, L. E. & Willander, M. Spin relaxation anisotropy in two-dimensional semiconductor systems. Preprint cond-mat/0202437 at ⟨http://xxx.lanl.gov⟩ (2002).
25. Averkiev, N. S. & D'yakonov, M. I. Current due to inhomogeneity of the spin orientation of electrons in a semiconductor. *Sov. Phys. Semicond.* **17,** 393–395 (1983).
26. Johnson, M. & Silsbee, R. H. Interfacial charge-spin coupling: injection and detection of spin magnetization in metals. *Phys. Rev. Lett.* **55,** 1790–1793 (1985).
27. Zutic, I., Fabian, J. & Das Sarma, S. Spin-polarized transport in inhomogeneous magnetic semiconductors: theory of magnetic/nonmagnetic *p–n* junctions. *Phys. Rev. Lett.* **88,** 066603-1–066603-4 (2001).

Acknowledgements

We thank D. I. Kovalev, W. Schoepe and M. Bichler for helpful discussions and support. We acknowledge financial support from the DFG, the RFFI and INTAS.

Competing interests statement

The authors declare that they have no competing financial interests.

Correspondence and requests for materials should be addressed to S.D.G. (e-mail: sergey.ganichev@physik.uni-regensburg.de).

Terahertz semiconductor-heterostructure laser

Rüdeger Köhler*, Alessandro Tredicucci*, Fabio Beltram*, Harvey E. Beere†, Edmund H. Linfield†, A. Giles Davies†, David A. Ritchie†, Rita C. Iotti‡ & Fausto Rossi‡

* *NEST-INFM and Scuola Normale Superiore, Piazza dei Cavalieri 7, 56126 Pisa, Italy*

† *Cavendish Laboratory, University of Cambridge, Madingley Road, Cambridge CB3 0HE, UK*

‡ *INFM and Dipartimento di Fisica, Politecnico di Torino, Corso Duca degli Abruzzi 24, 10129 Torino, Italy*

Semiconductor devices have become indispensable for generating electromagnetic radiation in everyday applications. Visible and infrared diode lasers are at the core of information technology, and at the other end of the spectrum, microwave and radio-frequency emitters enable wireless communications. But the terahertz region (1–10 THz; 1 THz = 10^{12} Hz) between these ranges has remained largely underdeveloped, despite the identification of various possible applications—for example, chemical detection, astronomy and medical imaging[1–4]. Progress in this area has been hampered by the lack of compact, low-consumption, solid-state terahertz sources[5–9]. Here we report a monolithic terahertz injection laser that is based on interminiband transitions in the conduction band of a semiconductor (GaAs/AlGaAs) heterostructure. The prototype demonstrated emits a single mode at 4.4 THz, and already shows high output powers of more than 2 mW with low threshold current densities of about a few hundred A cm^{-2} up to 50 K. These results are very promising for extending the present laser concept to continuous-wave and high-temperature operation, which would lead to implementation in practical photonic systems.

In conventional semiconductor lasers, light is generated by the radiative recombination of conduction band electrons with valence band holes across the bandgap of the active material; in contrast, electrons in a quantum-cascade laser propagate through a potential staircase of coupled quantum wells, where the conduction band is split by quantum confinement into a number of distinct sub-bands[10]. By choice of layer thickness and applied electric field, lifetimes and tunnelling probabilities of each level are engineered in order to obtain population inversion between two sub-bands in a series of identical repeat units. Injector/collector structures connect these active regions, allowing electrical transport through injection of carriers into the upper laser level, and extraction of carriers from the lower laser level. The radiation frequency is determined by the energy spacing of the lasing sub-bands, allowing in principle operation at arbitrarily long wavelengths. The quantum-cascade scheme has thus long been the preferred choice in many attempts to fabricate a terahertz semiconductor laser. Although electroluminescent devices have been reported by several groups[11–14], laser action has been shown only at much shorter wavelengths[15,16]. In fact, above the forbidden phonon band of the material, direct electron–longitudinal optical (LO) phonon scattering processes can be conveniently used to achieve large population inversions[16]. Furthermore, an additional problematic issue for the terahertz range stems from the fact that conventional laser waveguides are not suitable, owing to large free-carrier absorption losses and practical limitations on the thickness of epilayer growth.

As in all lasers, efficient depletion of the lower level is essential, and long lifetimes of the upper level are highly desirable. Up until now, proposed terahertz quantum-cascade designs focused mainly on the latter aspect. To this end, structures have featured narrow injector minibands to both suppress scattering of electrons from the

 © 2002 Macmillan Magazines Ltd

upper laser state through LO-phonon emission and block cross-absorption of the emitted light. This, however, results in relatively small tunnel coupling between the active region sub-bands and the injector states. As a consequence, extraction of carriers from the lower laser level is very slow, which, compounded with the limited current densities supported by the narrow injector minibands, hinders the achievement of population inversion[17]. On the contrary, our design targets precisely these two issues, an objective best fulfilled by the adoption of chirped superlattice active regions[18]. In particular, one repeat unit in our structure comprises seven GaAs quantum wells separated by $Al_{0.15}Ga_{0.85}As$ barriers, with the active region consisting of three closely coupled quantum wells.

A self-consistent calculation of the wavefunctions and energies in our device is shown in Fig. 1a, and details of the design are given in Fig. 1 legend. The lower laser state 1 is strongly coupled to a wide injector miniband, comprising seven sub-bands spanning an energy of 17 meV. This provides a large phase space where electrons scattered either from sub-band 2 or directly from the injector can spread, at the same time ensuring fast depletion of state 1. Moreover, the wide miniband allows efficient electrical transport, even at high current densities, and simultaneously suppresses thermal backfilling. The validity of this design is supported by theoretical modelling[17] employing a Monte Carlo scheme based on a coupled set of fully three-dimensional Boltzmann equations[19], including all relevant energy-relaxation mechanisms, like carrier–carrier and carrier–LO-phonon scattering processes[20]. The use of suitable periodic boundary conditions allows simulation of sub-band populations as well as current voltage characteristics without resorting to phenomenological parameters. The results displayed in Fig. 1b indeed predict the build-up of a significant population inversion above an applied electric field of $2\,kV\,cm^{-1}$, peaking at about $1.5 \times 10^9\,cm^{-2}$ just before the design field of $3.5\,kV\,cm^{-1}$. Large current densities of the order of $1\,kA\,cm^{-2}$ are also obtained before the onset of negative differential resistance that marks the end of resonant tunnelling transport. It is worth noting that, contrary to mid-infrared quantum-cascade lasers, where depletion of the lower laser state is controlled by optical phonon emission, in this case the

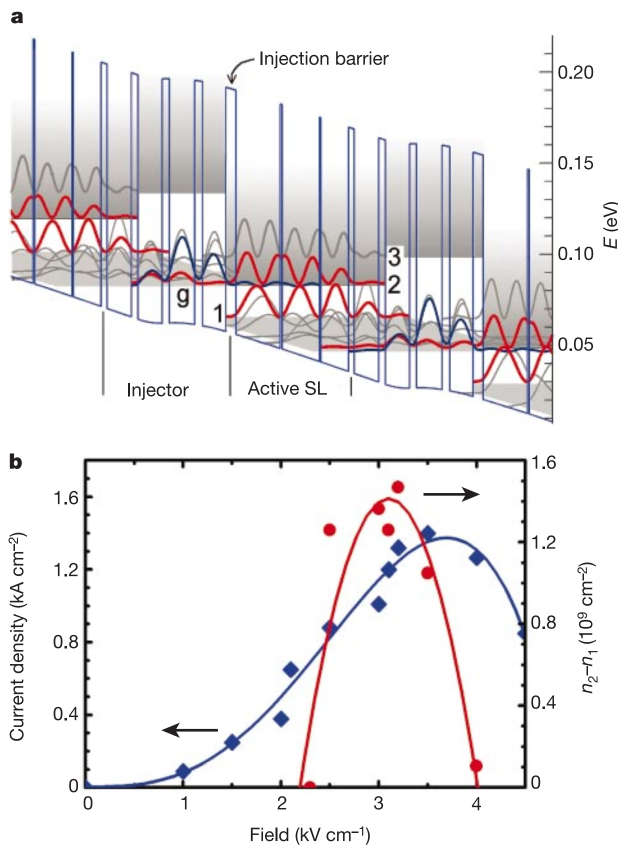

Figure 1 Conduction band structure of the laser active core and computed population inversion and current density at several applied biases. **a**, Self-consistent calculation of the conduction band structure of a portion of the layer stack in the waveguide core under a field of $3.5\,kV\,cm^{-1}$. Injectors and superlattice (SL) active regions are alternating. The layer thicknesses, in nm, starting from the injection barrier are ***4.3***/ *18.8*/ ***0.8***/ *15.8*/ ***0.6***/ *11.7*/ ***2.5***/ 10.3/ **2.9**/ 10.2/ **3.0**/ 10.8/ **3.3**/ 9.9, where $Al_{0.15}Ga_{0.85}As$ layers are in bold face, the active region is in italic, and the 10.2-nm-wide well is Si-doped at $4 \times 10^{16}\,cm^{-3}$. The moduli squared of the wavefunctions are shown, with miniband regions represented by shaded areas. The optical transition takes place across the 18-meV-wide minigap between the second and first miniband (states 2 and 1) and, being vertical in real space, presents a large dipole matrix element of 7.8 nm. Carriers are injected into state 2 via resonant tunnelling from the injector ground state labelled g. **b**, Calculated population inversion between states 2 and 1 of the active superlattice (circles), expressed in terms of electron sheet density (n_2 and n_1 respectively), and current density traversing the structure (diamonds). Both are computed as a function of bias field at 10 K. Solid lines are polynomial fits. From the simulation we also extract the level lifetimes: $\tau_2 = 0.8$ ps, $\tau_{21} = 8.3$ ps, $\tau_1 = 2.2$ ps with τ_2 and τ_{21} dominated by carrier-phonon scattering processes. Note that τ_{21} is much greater than τ_2 owing to the superlattice nature of the active region. This implies that $\tau_1 < \tau_{21}$, which is the necessary condition for population inversion.

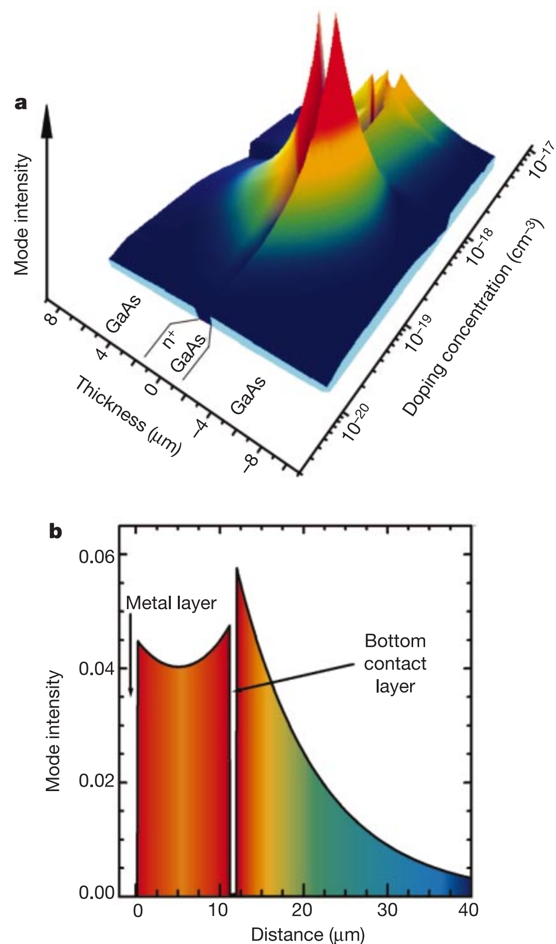

Figure 2 Waveguide design principle and radiation mode confinement. **a**, Evolution of the intensity profile of the optical mode bound to a 800-nm-thick GaAs n-doped layer within undoped GaAs material calculated as a function of donor density. The dielectric constants were derived from a Drude–Lorentz model. **b**, Calculated mode profile along the growth direction of the final device structure. The origin of the abscissa is at the top metal–semiconductor interface, and the waveguide core of 104 repetitions of the active region shown in Fig. 1 is between the bottom contact and top metal layer.

© 2002 Macmillan Magazines Ltd

transparency condition of the interminiband transition is reached at a current density significantly different from zero. Moreover, in our calculations population inversion is reached only in the presence of carrier–carrier scattering. This process provides the necessary in-plane momentum to activate relaxation of electrons in state 1 via carrier–phonon scattering[17].

As stated above, the waveguide is a very important aspect of the present device. Traditionally, long-wavelength quantum-cascade lasers exploit the surface plasmon mode at the interface between two materials with dielectric constants of opposite sign (normally a metal and a semiconductor) to achieve a tight optical confinement with low absorption losses[15,21]. At terahertz frequencies, however, a simple surface-plasmon waveguide results in a small overlap of the optical mode with any active region of reasonable thickness. Therefore, more sophisticated solutions have been considered, including double-surface plasmon structures where the guided mode is totally contained between two metallic claddings[22]. Here we have chosen to use a thin (800 nm) n^+ GaAs layer between 104 repeat periods of the above active superlattice on one side and an undoped GaAs substrate on the other in order to create a strongly confined low loss TM mode bound to that layer. This is a result of the n^+ layer dielectric constant (ε_A), which, by appropriately tuning the doping density, can be made negative, albeit comparable in modulus to that of the surrounding semiconductor (ε_B). The two surface plasmons existing at the two layer interfaces merge into a single mode because of the relatively small thickness of the n^+ layer with respect to the surface plasmon skin depth (δ_A):

$$\delta_A = \frac{\lambda}{2}\left|\mathrm{Re}\left[\varepsilon_A\sqrt{\frac{-1}{\varepsilon_A+\varepsilon_B}}\right]\right|^{-1}$$

The penetration of this mode into the outside semiconductor is at the same time minimized, being to a first approximation proportional to $\sqrt{-(\varepsilon_A+\varepsilon_B)}$, resulting in a very tight confinement.

In fact the situation is more intricate, owing to the complex nature of the dielectric constants, as can be seen in Fig. 2a where the evolution of the mode profile is plotted as a function of the n^+ layer doping density. We chose a donor density $n = 2\times10^{18}\,\mathrm{cm}^{-3}$, which yields a good compromise between absorption losses and overlap with the active material. Additionally this makes it possible to use the n^+ layer for electrical contacting. The presence on top of the active regions of a 200-nm-thick GaAs layer doped to $n = 5\times10^{18}\,\mathrm{cm}^{-3}$ with its metallic contact leads to the final mode profile of the actual device shown in Fig. 2b. A confinement factor $\Gamma = 0.47$ for the active material and an attenuation coefficient $\alpha_W = 16\,\mathrm{cm}^{-1}$ are computed, which are extremely favourable values at these long wavelengths.

The sample was grown by molecular beam epitaxy and further processed into mesa-etched ridge stripes by optical contact lithography and wet chemical etching. It was then thinned down to about 200 μm in order to improve heat dissipation, and top and bottom Ge/Au ohmic contacts were provided by thermal evaporation and subsequent annealing under a nitrogen atmosphere. A Fabry–Perot cavity was formed by cleaving the stripes into laser bars with the facets left uncoated. The devices were finally soldered, using an In-Ag alloy, onto a copper block, wire-bonded, and mounted onto the cold finger of a liquid-helium flow cryostat equipped with polyethylene windows.

Figure 3 shows the emission spectra of one such laser at 8 K for different drive currents. The characteristic narrowing of the emis-

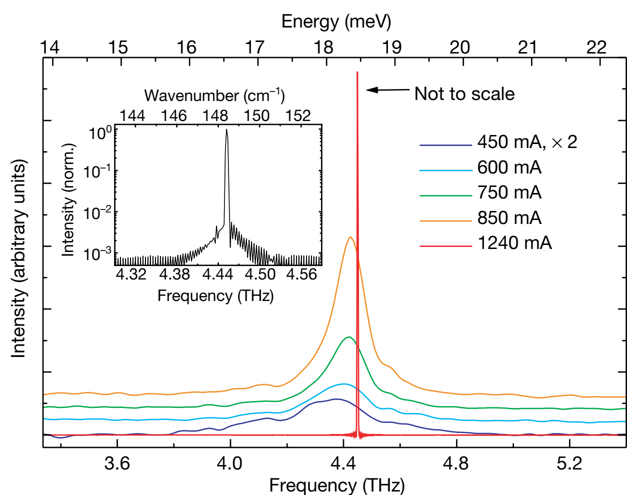

Figure 3 Emission spectra from a 1.24-mm-long and 180-μm-wide laser device recorded at 8 K for different drive currents. The lowest curve is multiplied by a factor of two for clarity, while the 1,240-mA laser spectrum (shown red) is scaled down by several orders of magnitude. Current macro-pulses were applied at a repetition rate of 333 Hz and matched the frequency response of the detector; each macro-pulse comprised 750 micro-pulses of 200 ns width at intervals of 2 μs to avoid excess heating in the device. The emitted radiation was collected by an *f*/1 off-axis parabolic mirror, passed through a Fourier-transform interferometer (FTIR) and focused again onto a liquid-helium-cooled Si bolometer. The entire beam path was purged with purified air in order to minimize water-vapour absorption. Subthreshold spectra were recorded with a resolution of $2\,\mathrm{cm}^{-1}$ (60 GHz) using the FTIR in step-scan mode and employing a lock-in amplifier for signal detection. The spontaneous emission at low drive currents (300 mA) displays a full-width at half-maximum of 2 meV, similar to the value obtained from previous luminescence structures with only 40 periods[23]. It is best fitted with a lorentzian line shape, which, together with the absence of any broadening when increasing the number of superlattice periods, indicates the high quality and uniformity of the growth throughout the whole 10-μm-thick active material stack. Laser spectra were collected in rapid-scan mode with the maximum possible resolution of $0.125\,\mathrm{cm}^{-1}$ (3.75 GHz) using a DTGS (deuterated triglycine sulphate) detector. Inset, the laser line on a logarithmic scale showing single-mode emission with a side-mode suppression ratio of 20 dB.

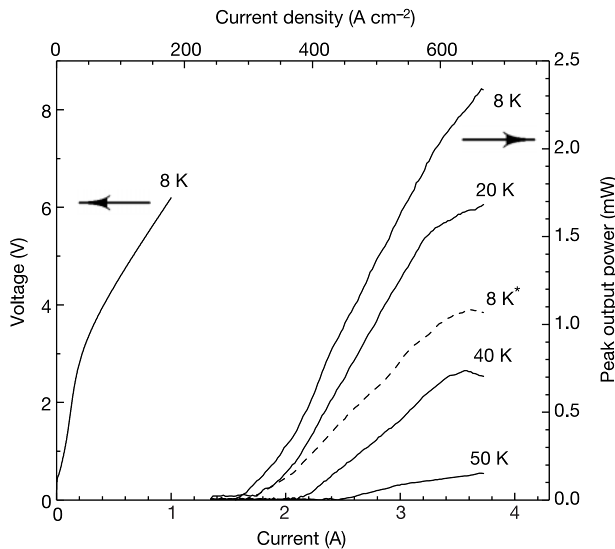

Figure 4 Light–current (*L–I*) characteristics of a 180-μm-wide and 3.1-mm-long laser ridge. Data were recorded in pulsed mode, applying 100-ns-long pulses at a repetition rate of 333 Hz. The peak power values represent what was collected from a single facet onto our detector after correction by a factor of 2 to account for the FTIR retro-reflection. At the lowest temperature the device emits more than 2 mW. When the duty cycle was increased to 0.5%, the peak power reduced to 1 mW owing to the stronger heating of the device, as shown by the dashed curve labelled with an asterisk. At the maximum operating temperature of 50 K, we observed 120 μW of peak output power. The optical output power was estimated using the responsivity of the bolometer as calibrated against black-body radiation by the manufacturer (QMC Instruments). The *V–I* curve at a temperature of 8 K is also displayed.

© 2002 Macmillan Magazines Ltd

sion line and nonlinear dependence of the intensity are clearly observed up to a current of about 880 mA, where laser threshold is reached. Lasing takes place at ~4.4 THz, on the high-energy side of the luminescence line, probably owing to the reduced waveguide losses at shorter wavelengths. Single-mode emission is obtained, which is probably a consequence of the relatively narrow gain spectrum and the wide Fabry–Perot mode spacing. A high-resolution laser spectrum is shown in the inset; the measured linewidth is limited by the resolution of the spectrometer (3.75 GHz).

Figure 4 shows the light–current (*L*–*I*) and voltage–current (*V*–*I*) characteristics of a representative device. At a heat-sink temperature of 8 K, the output peak power is estimated to be more than 2 mW, with a threshold current density of 290 A cm^{-2}. The latter is a very small value for quantum-cascade lasers and allows operation at high duty cycles (up to 10%) even in this large device. We expect that narrower stripes and appropriate changes in sample processing would readily lead to continuous-wave operation. The initial high resistivity in the *V*–*I* characteristics stems from misalignment of the sub-bands at low field; at higher fields, the injector miniband lines up with the second miniband of the following stage and carrier injection into the upper laser level takes place. The electric field at threshold is 7.5 kV cm^{-1}. This is larger than the design value of 3.5 kV cm^{-1}, probably as a result of the non-negligible contact resistance. As expected, a negative differential resistance feature was observed at about 850 A cm^{-2}.

These experimental results match well the theoretical predictions of Fig. 1b. The *V*–*I* curve has all the distinctive qualitative features and the measured current densities are of the same order of the computed ones, showing that even at these small energies carrier relaxation and transport are dominated by electron–LO phonon and electron–electron scattering. The discrepancy is a factor of about 1.5, possibly related to acoustic phonon or impurity scattering or to a lower than specified free-carrier density in the sample. In fact, the simulation indicates that a reduction in the doping density of the injectors by 25% would lead to a reduction in current density of 35%. From the theoretical values of population inversion and confinement factor, we calculate a maximum modal gain of 23 cm^{-1} (ref. 18). This value compares well with the estimated cavity losses $\alpha_W + \alpha_M = (16 + 4)\,cm^{-1} = 20\,cm^{-1}$, α_M being the mirror outcoupling of the 3.1-mm-long stripe. This consistency is confirmed by the experimental observation that laser stripes shorter than 1 mm, with corresponding larger mirror losses, do not reach laser threshold.

We believe that improved design of the active region of our device (in particular aiming at the reduction of thermal backfilling), together with optimized fabrication (junction-down mounting, facet coating, lateral overgrowth), would rapidly lead to continuous-wave emission and to operation at liquid-nitrogen temperatures. The present demonstration of a terahertz quantum-cascade laser, operating below the LO phonon band, represents a first step towards the development of widely usable terahertz photonics. □

Received 14 January; accepted 19 February 2002.

1. Miles, R. E., Harrison, P. & Lippens, D. (eds) *Terahertz Sources and Systems* Vol. 27 (NATO Science Series II, Kluwer, Dordrecht, 2001).
2. Han, P. Y., Cho, G. C. & Zhang, X.-C. Time-domain transillumination of biological tissue with terahertz pulses. *Opt. Lett.* **25,** 242–244 (2000).
3. Mittleman, D. M., Jacobsen, R. H. & Nuss, M. C. T-ray imaging. *IEEE J. Sel. Top. Quant. Electron.* **2,** 679–692 (1996).
4. Mittleman, D. M., Hunsche, S., Boivin, L. & Nuss, M. C. T-ray tomography. *Opt. Lett.* **22,** 904–906 (1997).
5. Pavlov, S. G. *et al.* Stimulated emission from donor transitions in silicon. *Phys. Rev. Lett.* **84,** 5220–5223 (2000).
6. Matsuura, S., Tani, M. & Sakai, K. Generation of coherent terahertz radiation by photomixing in dipole photoconductive antennas. *Appl. Phys. Lett.* **70,** 559–561 (1997).
7. Hu, B. B., Zhang, X.-C. & Auston, D. H. Terahertz radiation induced by subband-gap femtosecond optical excitation of GaAs. *Phys. Rev. Lett.* **67,** 2709–2712 (1991).
8. Kersting, R., Unterrainer, K., Strasser, G., Kauffmann, H. F. & Gornik, E. Few-cycle THz emission from cold plasma oscillations. *Phys. Rev. Lett.* **79,** 3038–3041 (1997).
9. Bründermann, E., Chamberlin, D. R. & Haller, E. E. High duty cycle and continuous terahertz emission from germanium. *Appl. Phys. Lett.* **76,** 2991–2993 (2000).
10. Faist, J. *et al.* Quantum cascade laser. *Science* **264,** 553–556 (1994).
11. Rochat, M., Faist, J., Beck, M., Oesterle, U. & Ilegems, M. Far-infrared (λ = 88 μm) electroluminescence in a quantum cascade structure. *Appl. Phys. Lett.* **73,** 3724–3726 (1998).
12. Williams, B. S., Xu, B., Hu, Q. & Melloch, M. R. Narrow-linewidth terahertz intersubband emission from three-level systems. *Appl. Phys. Lett.* **75,** 2927–2929 (1999).
13. Ulrich, J., Zobl, R., Schrenk, W., Strasser, G. & Unterrainer, K. Terahertz quantum cascade structures: Intra- versus interwell transition. *Appl. Phys. Lett.* **76,** 1928–1930 (2000).
14. Helm, M., England, P., Colas, E., De Rosa, F. & Allen, S. J. Intersubband emission from semiconductor superlattices excited by sequential resonant tunnelling. *Phys. Rev. Lett.* **63,** 74–77 (1989).
15. Colombelli, R. *et al.* Far-infrared surface-plasmon quantum-cascade lasers at 21.5 μm and 24 μm wavelengths. *Appl. Phys. Lett.* **78,** 2620–2622 (2001).
16. Hofstetter, D., Beck, M., Aellen, T. & Faist, J. High-temperature operation of distributed feedback quantum-cascade lasers at 5.3 μm. *Appl. Phys. Lett.* **78,** 396–398 (2001).
17. Köhler, R., Iotti, R. C., Tredicucci, A. & Rossi, F. Design and simulation of terahertz quantum cascade lasers. *Appl. Phys. Lett.* **79,** 3920–3922 (2001).
18. Tredicucci, A. *et al.* High performance interminiband quantum cascade lasers with graded superlattices. *Appl. Phys. Lett.* **73,** 2101–2103 (1998).
19. Iotti, R. C. & Rossi, F. Nature of charge transport in quantum-cascade lasers. *Phys. Rev. Lett.* **87,** 146603-1–146603-4 (2001).
20. Iotti, R. C. & Rossi, F. Carrier thermalization versus phonon-assisted relaxation in quantum-cascade lasers: A Monte Carlo approach. *Appl. Phys. Lett.* **78,** 2902–2904 (2001).
21. Sirtori, C. *et al.* Long-wavelength (λ ~ 8–11.5 μm) semiconductor lasers with waveguides based on surface plasmons. *Opt. Lett.* **23,** 1366–1368 (1998).
22. Rochat, M., Beck, M., Faist, J. & Oesterle, U. Measurement of far-infrared waveguide loss using a multisection single-pass technique. *Appl. Phys. Lett.* **78,** 1967–1969 (2001).
23. Köhler, R. *et al.* High-intensity interminiband terahertz emission from chirped superlattices. *Appl. Phys. Lett.* **80,** 1867 (2002).

Acknowledgements

We thank S. Dhillon for discussions.This work was supported in part by the European Commission through the IST Framework V FET project WANTED. R.K. was supported by the C.N.R.; E.H.L. and A.G.D were supported by Toshiba Research Europe Ltd and The Royal Society, respectively.

Competing interests statement

The authors declare that they have no competing financial interests.

Correspondence and requests for materials should be addressed to R.K. (e-mail: koehler@nest.sns.it.).

Ocean productivity before about 1.9 Gyr ago limited by phosphorus adsorption onto iron oxides

Christian J. Bjerrum*†‡ **& Donald E. Canfield***

* *Danish Center for Earth System Science, Institute of Biology, University of Southern Denmark, Campusvej 55, DK-5230 Odense, Denmark*

† *Danish Center for Earth System Science, Niels Bohr Institute for Astronomy, Physics and Geophysics, University of Copenhagen, Juliane Maries Vej 30, DK-2100 Copenhagen, Denmark*

After the evolution of oxygen-producing cyanobacteria at some time before 2.7 billion years ago[1], oxygen production on Earth is thought to have depended on the availability of nutrients in the oceans, such as phosphorus (in the form of orthophosphate). In the modern oceans, a significant removal pathway for phosphorus occurs by way of its adsorption onto iron oxide deposits[2,3]. Such deposits were thought to be more abundant in the past when, under low sulphate conditions, the formation of large amounts of iron oxides resulted in the deposition of banded iron formations[4,5]. Under these circumstances, phosphorus removal by iron oxide adsorption could have been enhanced. Here we analyse the phosphorus and iron content of banded iron formations to show that ocean orthophosphate concentrations from

‡ Present address: Geological Institute, University of Copenhagen, Øster Voldgade 10, DK-1350 Copenhagen, Denmark.

 © 2002 Macmillan Magazines Ltd